In-plane strain-free stanene on a Pd$_2$Sn(111) surface alloy

Junji Yuhara [1,*] Tsuyoshi Ogikubo,[1] Masaaki Araidai,[1,2] Sho-ichi Takakura,[3,4] Masashi Nakatake,[4] and Guy Le Lay [5]

[1]*Graduate School of Engineering, Nagoya University, Nagoya 464-8603, Japan*
[2]*Institute of Materials and Systems for Sustainability, Nagoya University, Nagoya 464-8601, Japan*
[3]*Synchrotron Radiation Research Center, Nagoya University, Nagoya 464-8603, Japan*
[4]*Aichi Synchrotron Radiation Center, Seto 489-0965, Japan*
[5]*Aix-Marseille Université, CNRS, PIIM UMR 7345, 13397 Marseille Cedex, France*

Here we report the growth of laterally strain-free stanene, that is a two-dimensional (2D) honeycomb structure of tin atoms, on a Pd(111) crystal terminated by a Pd$_2$Sn surface alloy. The atomic geometry and the electronic structure have been thoroughly investigated by scanning tunneling microscopy (STM), low-energy electron diffraction (LEED), Auger electron spectroscopy, high-resolution synchrotron radiation photoemission spectroscopy, and advanced first principles calculations. The STM images clearly reveal the epitaxial growth of honeycomb stanene on the preformed Pd$_2$Sn surface alloy. LEED patterns clearly show commensurate $(\sqrt{3}\times\sqrt{3})$R30° spots, corresponding to a lattice constant of 0.47 nm, in perfect accord with the cell size of free-standing stanene. The measured very low buckling, within 20 pm, is derived from section profiles of atomic-scale STM images. This contrasts the significantly larger buckling of free-standing stanene, possibly due to a STM tip effect as well as a non-negligible interaction with the underlying surface alloy. The electronic structure exhibits a characteristic 2D band with parabolic dispersion, which is in good accordance with electronic structure calculations in density functional theory.

I. INTRODUCTION

After the pioneering synthesis in 2012 of silicene on the (111) surfaces of silver single crystals and the (0001) surfaces of epitaxial ZrB$_2$ thin films [1–4], Group 14 post-graphene monoelemental artificial two-dimensional (2D) structures have received tremendous attention both from the theoretical viewpoint and the experimental investigations of the growth processes as well as the characterization [5–12]. Among the post-graphene materials, stanene has attracted particular interest because of its exotic properties possibly made available at room temperature. Indeed, unique physical properties have been predicted for stanene, such as the quantum spin Hall effect [13,14], giant magnetoresistance [15], and anomalous Seebeck effect [16].

Epitaxial growth of stanene has been achieved on several substrates yielding different characteristics. In terms of buckling, the stanene sheets prepared on Bi$_2$Te$_3$(111) and Ag(111) surfaces, respectively, show 120 and 12 pm corrugations, as estimated from scanning tunneling microscopy (STM) images, [8,17], while free-standing stanene itself (sometimes called tinene) has a calculated intrinsic buckling of 85 pm [18]. The lattice sizes of stanene prepared on Sb(111) and Bi$_2$Te$_3$(111), on the one hand, are 0.43 and 0.44 nm, respectively, somewhat smaller than that of free-standing stanene, whose calculated lattice parameter is 0.47 nm [8,18,19]. On the other hand, the lattice sizes of the stanene layers prepared on Ag(111) and Cu(111) are, instead, relatively larger,

namely, 0.50 nm and 0.51 nm, respectively, reflecting the associated supercell match with each substrate, either with $(\sqrt{3}\times\sqrt{3})$R(30°) or (2 × 2) periodicities [17,20]. The lattice sizes and bucklings of stanene are summarized in Table I.

When stanene will be detached to be transferred to convenient templates, it would be certainly better to start from a stanene sheet having a 2D lattice constant similar to that of free-standing stanene. It is established that deposition of Sn films onto Pd(111) leads to the formation of a Pd$_2$Sn surface alloy with $(\sqrt{3}\times\sqrt{3})$ periodicity related to the substrate [21–23], and a lattice size of 0.47 nm, in perfect correspondence with that of free-standing stanene. This is why we use a Pd(111) crystal and prepare a $(\sqrt{3}\times\sqrt{3})$ Pd$_2$Sn surface alloy as an initial substrate.

In the following, we will demonstrate the large-area epitaxial growth of well-ordered and laterally strain-free stanene on the Pd$_2$Sn surface alloy prepared on Pd(111). We will examine the geometrical and electronic structures using in synergy low-energy electron diffraction (LEED) and STM observations together with angle-resolved photoemission spectroscopy (ARPES) measurements, along with density functional theory (DFT) calculations for the atomic and electronic structures.

II. EXPERIMENT AND CALCULATION

The experiments were performed using two ultrahigh-vacuum systems at Nagoya University and at the Aichi synchrotron radiation center. Each system consisted of a preparation chamber with a base pressure below 5 ×

*Corresponding author: j-yuhara@energy.nagoya-u.ac.jp

TABLE I. The lattice sizes and bucklings of stanene formed on different substrates.

Substrate	Lattice size (nm)	Buckling height Δ (pm)
Sb(111) [19]	0.43	20
$Bi_2Te_3(111)$ [8]	0.44	120
Free-standing [18]	0.47	85
Pd(111)	0.48 ($\sqrt{3}\times\sqrt{3}$)	20
Ag(111) [10]	0.50 ($\sqrt{3}\times\sqrt{3}$)	<12
Cu(111) [20]	0.51 (2×2)	0

10^{-10} mbar, and an analysis chamber with a base pressure below 10^{-10} mbar.

The system was equipped with a rear-view LEED system operating with a LaB_6 filament and a UHV STM system at Nagoya University. All STM images were acquired at room temperature (RT) with W tips. All apparatuses were situated on an air damper with an active vibration isolation system. The core-level photoemission spectroscopy (CLS) and ARPES experiments were performed at RT at the Aichi synchrotron radiation center, where the vessel was equipped with a rear view LEED instrument with a microchannel-plate intensified detector (MCP-LEED) and a 200 mm-radius hemispherical photoelectron analyzer. The overall resolution was better than 50 meV. The palladium sample was mounted in a manipulator with 4-axis pulse motor control.

Clean Pd(111) surfaces were prepared by 2-keV Ar^+ ion sputtering at room temperature followed by annealing up to 900 °C. The cleanliness of the surface was checked by Auger electron spectroscopy after sputtering and annealing; no contaminants, such as C and O, were observed within the detection limits, and a sharp (1×1) LEED pattern was observed. Tin was deposited onto the Pd(111) surface at various temperatures up to 500 °C in UHV from a well degassed quartz crucible evaporator operating at a deposition rate of approximately 0.11 monolayer (ML)/min, as measured by placing a quartz crystal microbalance at the sample position. We define 1 ML as a Sn overlayer with the atomic density of a Pd(111) plane: 1.53×10^{15} atoms/cm². The deposition rate was accurately calibrated by Rutherford backscattering spectroscopy (RBS). For the RBS measurement, we prepared a graphite substrate with an ultrathin tin film on the surface. Details of the experimental setup for RBS have been published elsewhere [24].

The DFT calculations were performed with the QuantumATK version R-2020.09-SP1, Synopsys QuantumATK [25]. We used pseudoatomic orbitals as the basis functions. The interactions between ionic core and valence electrons were described by optimized norm-conserving Vanderbilt (ONCV) pseudopotentials of the PseudoDojo project [26] and Perdew-Burke-Ernzerhof-type exchange-correlation energy functionals were also employed [27]. The calculations have been performed for an hexagonal lattice with basis vectors $(a, b) = (4.765, 4.765)$ in unit of Å; periodic boundary conditions were imposed along both directions. In the c direction, one side of the slab consisting of 12 atomic layers was coupled to a semi-infinite Pd(111) electrode as the boundary
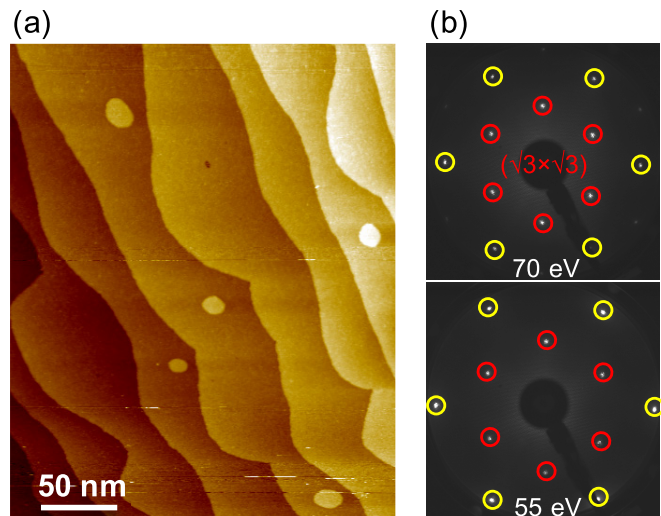

FIG. 1. (a) Large-scale STM image ($U_s = +1.2$ V, I $= 200$ pA) of the Pd_2Sn surface alloy prepared on a Pd(111) single crystal upon Sn deposition of 0.4 ML at RT with post annealing at 430 °C. (b) LEED patterns at 70 and 55 eV incident electron energy of the Ag_2Sn surface alloy. The primitive spots for Pd(111) are marked with yellow circles.

condition by the Green's function technique [28], and the opposite side had a vacuum region of about 18 Å. The atomic configuration except for six layers close to the electrode was relaxed until the forces acting on atoms became smaller than 10 meV/Å. The cutoff energy for space discretization was taken to be 2721 eV. The Brillouin zone (BZ) of the unit cell was sampled with a $9 \times 9 \times 1\Gamma$-center k-point grid.

III. EXPERIMENTAL RESULTS AND DISCUSSION

Figure 1 shows an experimental STM image and LEED patterns of the Pd_2Sn surface alloy prepared on a Pd(111) single crystal with a Sn deposition of 0.4 ML at 430 °C. The wide scale STM image in Fig. 1(a) shows a single atomic step, 0.23 ± 0.01 nm high, which corresponds to a monoatomic palladium step, separating two wide terraces with a few 2D islands. Typically, the average width of the terraces is more than 50 nm. The LEED patterns, displaying sixfold symmetry at variance with the threefold one of the bare Pd(111) substrate, clearly exhibit $\sqrt{3}\times\sqrt{3}$ spots, as shown in Fig. 1(b). The intensities of the $\sqrt{3}\times\sqrt{3}$ spots do not depend on the incident electron energy, indicating that the Pd_2Sn surface alloy has a 2D structure. These results are consistent with previous works reporting that a Pd_2Sn surface alloy is formed with $\sqrt{3}\times\sqrt{3}$ periodicity, notably upon Sn deposition of 1/3 ML onto the Pd(111) kept at 700 K [21].

Figure 2 shows an experimental STM image and LEED patterns of the Sn film deposited onto the Pd_2Sn surface alloy for an additional 0.7 ML deposited at RT and post-annealed at 350 °C. We find that an atomically thin film grows two dimensionally on this Pd_2Sn surface alloy, not only from the substrate steps but also on the terrace, as shown in Fig. 2(a). Since this atomic layer presents some holes in addition to 2D islands, it is obvious that the next layer grows before completing the entire sheet. Therefore, the films basically adopt
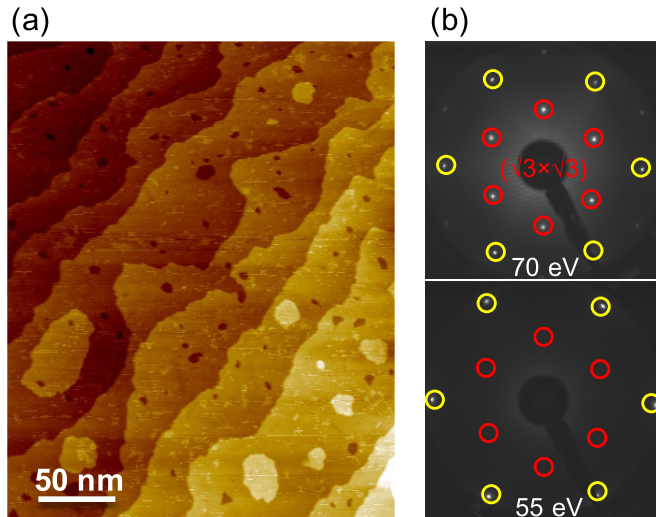
FIG. 2. (a) Large-scale STM image (U_s = +1.2 V, I = 200 pA) of stanene prepared on a Pd$_2$Sn surface alloy upon Sn deposition of 0.7 ML at RT with post annealing at 350 °C. (b) Corresponding LEED patterns at 70 eV and 55 eV incident electron energy. The primitive spots for Pd(111) are marked with yellow circles.

a laminar growth mode. The corresponding LEED pattern exhibits only $\sqrt{3}\times\sqrt{3}$ spots, as shown in Fig. 2(b), again with sixfold symmetry, yet, their intensities at different energies differ significantly from those of the initial Pd$_2$Sn surface alloy, which allows easy distinction, especially, there is almost no intensity for the $\sqrt{3}\times\sqrt{3}$ spots at 55 eV incident energy. It turns out that a similar energy dependence of the $\sqrt{3}\times\sqrt{3}$ spot intensities is observed for stanene on an Ag$_2$Sn surface alloy [17].

Figure 3 shows a middle-scale STM image of the Sn film deposited onto the Pd$_2$Sn surface alloy for an additional 0.5 ML at RT and postannealing at 380 °C. The close-up STM image from the uncovered part of the Pd$_2$Sn surface alloy area exhibits just a single bright spot per $\sqrt{3}\times\sqrt{3}$ unit cell [Fig. 3(b)], as expected from the results mentioned above. Close-up STM images from the areas covered by the Sn film clearly reveal a striking honeycomb structure [Fig. 3(c)]. The section profiles indicate that its lattice constant is 0.47 nm while the height difference between Sn atoms is only about 20 pm [Figs. 3(d)–3(e)]. Close-up STM images taken at a negative sample bias show a quite similar appearance of the stanene layer in filled states [29]. One can thus infer that laterally strain-free stanene with low buckling is formed, growing in a 2D island mode on the Ag$_2$Sn surface alloy.

Figure 4(a) shows the high-resolution Sn 4d spectra of the Pd$_2$Sn surface alloy, prepared by the Sn deposition of 0.4 ML on the Pd(111) with postannealing at 430 °C, and those from the stanene sheet grown on top obtained by the next Sn deposition of 0.5 ML at RT and postannealing at 380 °C. The Sn 4d spectrum for the surface alloy exhibits at first sight a single component with just a slight tailing at higher binding energy (BE). However, a thorough decomposition indicates that there are in reality two components, namely A1 and A2. The dominant component A1 originates from the surface alloy, while the A2 one is assigned to a small contribution of the stanene sheet, as described below. The Sn 4d spectrum for
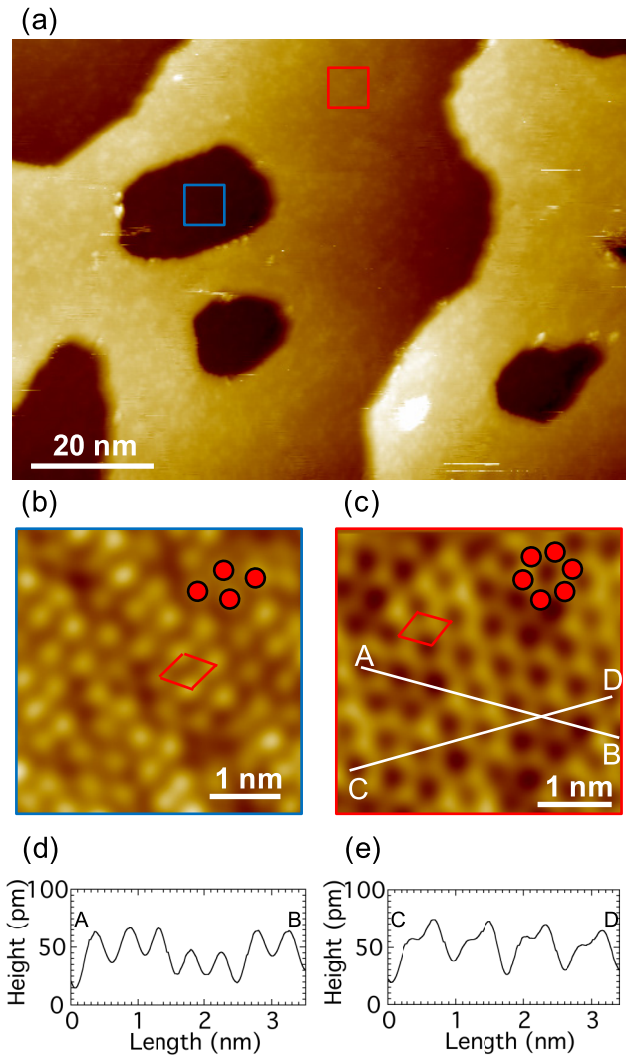

FIG. 3. (a) Large-scale STM image of stanene prepared on a Pd$_2$Sn surface alloy upon Sn deposition of 0.5 ML at RT with post annealing at 380 °C. The image is recorded in constant current mode with tunneling current of 200 pA and sample bias of +1.0 V. High-resolution STM images of (b) Pd$_2$Sn surface alloy (U_s = +0.8 V, I = 200 pA) and (c) stanene (U_s = +0.9V, I = 200 pA), which are observed in the blue and red line square in (a). (d), (e) Section profiles along the A-B and C-D lines in (d).

stanene grown on the surface alloy exhibits a clear shoulder at higher BE, indicating that there are two components, namely S1 and A2, separated by 0.27 eV. Because the high-resolution STM images display dominantly the stanene sheet, while the remaining areas concern the Pd$_2$Sn surface alloy, the S1 and A2 components are unambiguously associated to the stanene sheet and the Pd$_2$Sn surface alloy, from the comparison of the respective intensities. The nominal intensity ratio for stanene (2/3 ML) and the surface alloy (1/3 ML) is 2, while the measured intensity ratio for S1 to A2 is 2.45, indicating, as expected, that the Pd$_2$Sn surface alloy is not totally covered by stanene. While the measured buckling of stanene is about 20 pm, the chemical environments for Sn atoms (A and B sites) are considered to be the same. Here, it is worth noting that the Sn bonding environment for stanene on the Pd$_2$Sn surface
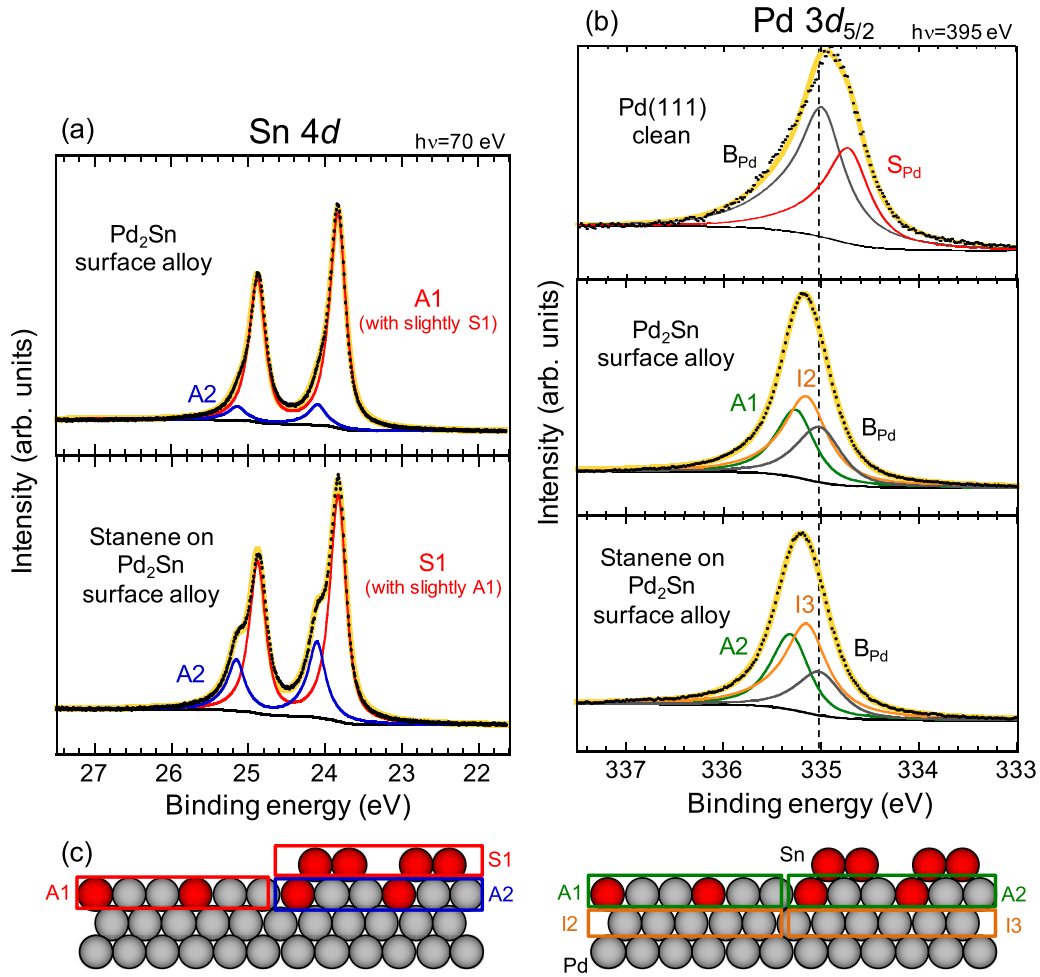
FIG. 4. High-resolution synchrotron radiation Sn $4d$ and Pd $3d_{5/2}$ core-level spectra measured at RT and taken at hν = 70 and 395 eV, respectively. (a) Sn $4d$ and (b) Pd $3d_{5/2}$ for clean bare Pd(111) single crystal, for a Pd$_2$Sn surface alloy at a Sn coverage of 0.4 ML, and for stanene prepared on this Pd$_2$Sn surface alloy with further Sn deposition of 0.5 ML at RT and post-annealing at 350 °C. S, A, I, are the components related to stanene, the surface alloy, the interface, while S$_{Pd}$ and B$_{Pd}$ correspond to the Pd surface component and the Pd bulk one at 335.0 eV binding energy (pinpointed by the vertical line), respectively. Each suffix number represents the layer number from top to down. (c) Scheme of the surface alloy and the stanene overlayer (side views), referencing each component.

alloy is basically the same as that for stanene on the Ag$_2$Sn surface alloy [17].

Figure 4(b) shows the corresponding high-resolution Pd $3d_{5/2}$ spectra of Fig. 4(a) with the spectrum from the clean Pd(111) as a reference. The spectra for the Pd$_2$Sn surface alloy and the differently prepared stanene layers exhibit similar full width at half maximums and are slightly narrower than the spectrum from the clean bare Pd(111) surface, which comprises a surface component, S$_{Pd}$, in addition to the bulk component B$_{Pd}$. For the Pd$_2$Sn surface alloy itself, three components are needed for the fit, related to palladium in the Pd$_2$Sn surface alloy (A1), to the palladium layer beneath the surface alloy (I2), and, to the bulk component (B$_{Pd}$), indeed always located at the same BE. Once the initially formed Pd$_2$Sn surface alloy is covered by the stanene layer, the original A1 component shifts slightly (by 0.05 eV) toward higher BE because of the different environment; it is renamed as the A2 component. In addition, the intensity of the B$_{Pd}$ component decreases because of the short electron escape depth. Therefore, the Pd $3d_{5/2}$ spectrum is considered to comprise three

components stemming from the Pd$_2$Sn surface alloy (A2), from the palladium layer beneath the surface alloy (I3), and from the bulk component (B$_{Pd}$). Side view illustrations of the surface alloy and the stanene overlayer are shown in Fig. 4(c) with indications of the origin of each component. Again, the Pd bonding environment for stanene on the Pd$_2$Sn surface alloy is basically similar to that for stanene on the Ag$_2$Sn surface alloy [17].

Hence, from the synchrotron radiation CLS detailed signatures, in synergy with the acquired STM images and the different intensities noticed in the LEED patterns (see above), we can unambiguously conclude that stanene has been formed on top of an Pd$_2$Sn surface alloy.

This assertion is further confirmed by our DFT calculations (basically in accord with previous ones for the Pd($\sqrt{3} \times \sqrt{3}$)R(30°) reconstruction associated with the Pd$_2$Sn surface alloy [23]. In Fig. 5 we show the calculated atomic structure of the epitaxial stanene sheet overlaying the Pd$_2$Sn surface alloy. The average vertical distance between the stanene sheet and the ($\sqrt{3} \times \sqrt{3}$)R(30°) surface alloy is
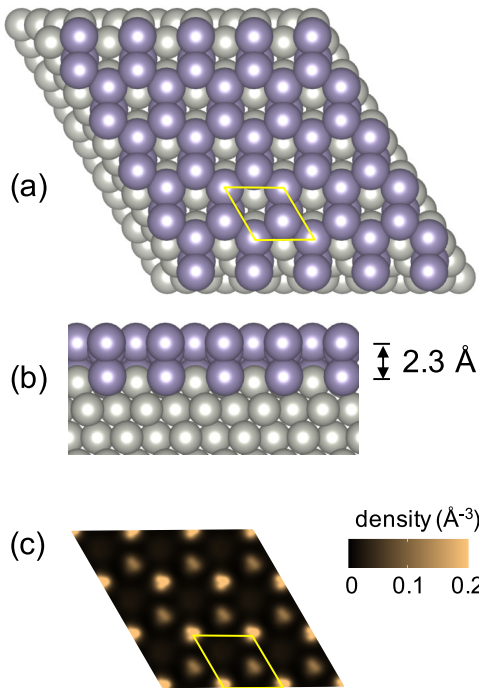
FIG. 5. Top (a) and side (b) views of the DFT calculated atomic geometry of stanene on the preformed Pd₂Sn surface alloy on Pd(111). Tin and silver atoms are shown as purple and silver balls, respectively. (c) Corresponding simulated STM image.

0.23 nm. The buckling of the stanene overlayer is 62 pm, larger than the experimental value of just 20 pm, surely underevaluated due to tip effects (convolution of geometric and electronic effects) and possibly atom thermal vibration effects since STM measurements are performed at RT.

Constant energy maps at the Fermi level for the stanene overlayer grown on the Pd₂Sn surface alloy are displayed at 70-eV photon energy in Figs. 6(a). The large black hexagon represents the Pd(111)(1 × 1) surface BZ, while the smaller red ones correspond to the 1 × 1 BZ of stanene, matching the Pd($\sqrt{3} \times \sqrt{3}$)R(30°) reconstruction associated with the stanene on the Pd₂Sn surface alloy. A specific structure with triangular warping is observed around the Γ point for the stanene sheet. Figure 6(b) shows the band structures of the stanene on the Pd₂Sn surface alloy, measured by ARPES at a photon energy of 70 eV along the K$_{Pd}$-Γ-K$_{Pd}$/M$_{Stanene}$-Γ-M$_{Stanene}$ direction. For the stanene sheet, in addition to the Pd related bands, a new band structure with parabolic dispersion is clearly recognized around Γ.

Figures 7(a) and 7(b) show the calculated band structures for the Pd₂Sn surface alloy and the stanene overlayer on the Pd₂Sn surface alloy. The parabolic band around the Γ point, originating from Sn sp orbitals, is only observed for the stanene sheet overlaying the Pd₂Sn surface alloy. Figures 7(c)–7(d) show the section profiles of corresponding electron localization functions passing through a tin atom of stanene. It is recognized that there is a weak interaction between the stanene sheet and the Pd₂Sn surface alloy. Therefore, the parabolic band arises after the stanene epitaxial growth, providing its signature, maybe that of a 2D interface state. However, the minimum of this band is shifted by 0.7 eV
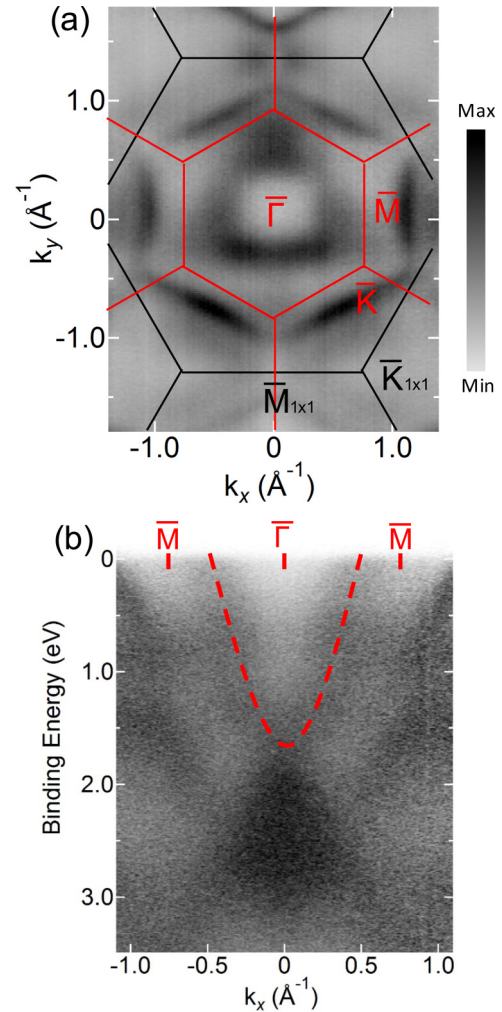

FIG. 6. Band structures of stanene prepared on a Pd₂Sn surface alloy. (a) Constant energy contours obtained at the binding energy of 0.1 eV, within an interval of ±0.05 eV. The first Brillouin zones of Pd(111) and the stanene sheet over the ($\sqrt{3} \times \sqrt{3}$)R30° Pd₂Sn surface alloy are drawn in black and red, respectively. (b) Corresponding ARPES intensity plot as measured along the common Pd(111) K̄-Γ̄-K̄ and stanene M̄-Γ̄-M̄ directions.

compared to the measurements, which must be due to many body effects, not taken into account in the calculations.

Finally, we want to emphasize the key result we have obtained, namely the growth of laterally strain-free stanene using Pd(111) as an initial substrate. When one will wish to transfer a stanene overlayer on another surface, it will be essential to prepare such a laterally strain-free stanene sheet. Otherwise, the shrinking or expanding stress for stanene could induce detrimental bond breaking. Therefore, the present result removes one of the major obstacles for stanene detachment.

IV. CONCLUSIONS

In summary, laterally strain-free stanene has been synthesized on a Pd₂Sn surface alloy preprepared on Pd(111). This strain-free stanene has been identified and characterized by several methods combined in synergy, using STM, LEED, and ARPES, along with DFT calculations. The geometry of the
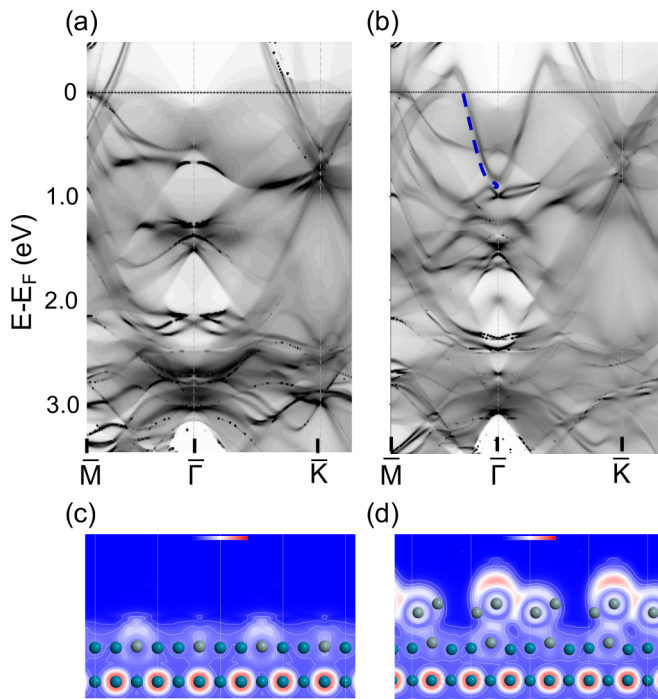
FIG. 7. DFT band structures of (a) a Pd_2Sn surface alloy and (b) a stanene sheet in epitaxy on the Pd_2Sn surface alloy. (c), (d) Corresponding electron localization functions passing through the tin atoms of stanene.

stanene sheet prepared on a Pd(111) crystal is quite similar to that of stanene on Ag(111), except for the lattice size. Compared to free standing stanene, the measured buckling is less, this, probably being related to the thermal vibrations and tip effects as well as a non-negligible interaction with the underlying surface alloy. A parabolic 2D band structure around the BZ center has been determined, possibly pointing to an interface band. Laterally strain-free stanene is considered to be most promising for realizing electronically free standing stanene upon detachment.

[1] P. Vogt, P. De Padova, C. Quaresima, J. Avila, E. Frantzeskakis, M. C. Asensio, A. Resta, B. Ealet, and G. Le Lay, Silicene: Compelling Experimental Evidence for Graphenelike Two-Dimensional Silicon, Phys. Rev. Lett. **108**, 155501 (2012).

[2] C.-L. Lin, R. Arafune, K. Kawahara, N. Tsukahara, E. Minamitani, Y. Kim, N. Takagi, and M. Kawai, Structure of Silicene Grown on Ag(111), Appl. Phys. Express **5**, 045802 (2012).

[3] B. Feng, Z. Ding, S. Meng, Y. Yao, X. He, P. Cheng, L. Chen, and K. Wu, Evidence of silicene in honeycomb structures of silicon on Ag(111), Nano Lett. **12**, 3507 (2012).

[4] A. Fleurence, R. Friedlein, T. Ozaki, H. Kawai, Y. Wang, and Y. Yamada-Takamura, Experimental Evidence for Epitaxial Silicene on Diboride Thin Films, Phys. Rev. Lett. **108**, 245501 (2012).

[5] K. Takeda and K. Shiraishi, Theoretical possibility of stage corrugation in Si and Ge analogs of graphite, Phys. Rev. B **50**, 14916 (1994).

[6] S. Cahangirov, M. Topsakal, E. Aktürk, H. Şahin, and S. Ciraci, Two- and One-Dimensional Honeycomb Structures of Silicon and Germanium, Phys. Rev. Lett. **102**, 236804 (2009).

[7] M. E. Dávila, L. Xian, S. Cahangirov, A. Rubio, and G. Le Lay, Germanene: A novel two-dimensional Germanium Allotrope Akin to Graphene and Silicene, New J. Phys. **16**, 095002 (2014).

[8] F. Zhu, W. Chen, Y. Xu, C. Gao, D. Guan, C. Liu, D. Qian, S.-C. Zhang, and J. Jia, Epitaxial growth of two-dimensional stanene, Nat. Mater. **14**, 1020 (2015).

[9] J. Yuhara, B. He, N. Matsunami, M. Nakatake, and G. Le Lay, Graphene's latest cousin: Plumbene epitaxial growth on a "nano watercube, Adv. Mater. **31**, 1901017 (2019).

[10] J. Yuhara, H. Shimazu, K. Ito, A. Ohta, M. Araidai, M. Kurosawa, M. Nakatake, and G. Le Lay, Germanene epitaxial growth by segregation through Ag(111) thin films on Ge(111), ACS Nano **12**, 11632 (2018).

[11] T. Ogikubo, H. Shimazu, Y. Fujii, K. Ito, A. Ohta, M. Araidai, M. Kurosawa, G. Le Lay, and J. Yuhara, Continuous growth of germanene and stanene lateral heterostructures, Adv. Mater. Interfaces **7**, 1902132 (2020).

[12] J. Yuhara and G. Le Lay, Beyond silicene: Synthesis of germanene, stanene and plumbene, Jpn. J. Appl. Phys. **59**, SN0801 (2020).

[13] Y. Xu, B. Yan, H.-J. Zhang, J. Wang, G. Xu, P. Tang, W. Duan, and S.-C. Zhang, Large-Gap Quantum Spin Hall Insulators in Tin Films, Phys. Rev. Lett. **111**, 136804 (2013).

[14] Y. Fang, Z.-Q. Huang, C.-H. Hsu, X. Li, Y. Xu, Y. Zhou, S. Wu, F.-C. Chuang, and Z.-Z. Zhu, Quantum spin hall states in stanene/Ge(111), Sci. Rep. **5**, 14196 (2015).

[15] S. Rachel and M. Ezawa, Giant magnetoresistance and perfect spin filter in silicene, germanene, and stanene, Phys. Rev. B **89**, 195303 (2014).

[16] Y. Xu, Z. Gan, and S.-C. Zhang, Enhanced Thermoelectric Performance and Anomalous Seebeck Effects in Topological Insulators, Phys. Rev. Lett. **112**, 226801 (2014).

[17] J. Yuhara, Y. Fujii, K. Nishino, N. Isobe, M. Nakatake, L. Xian, A. Rubio, and G. Le Lay, Large area planar

stanene epitaxially grown on Ag(111), 2D Mater. **5**, 025002 (2018).

[18] L. Matthes, O. Pulci, and F. Bechstedt, Massive dirac quasi-particles in the optical absorbance of graphene, silicene, germanene, and tinene, J. Phys. Condens. Matter **25**, 395305 (2013).

[19] J. Gou, L. Kong, H. Li, Q. Zhong, W. Li, P. Cheng, L. Chen, and K. Wu, Strain-induced band engineering in monolayer stanene on Sb(111), Phys. Rev. Mater. **1**, 054004 (2017).

[20] J. Deng, B. Xia, X. Ma, H. Chen, H. Shan, X. Zhai, B. Li, A. Zhao, Y. Xu, W. Duan, S.-C. Zhang, B. Wang, and J. G. Hou, Epitaxial growth of ultraflat stanene with topological band inversion, Nat. Mater. **17**, 1081 (2018).

[21] A. F. Lee, C. J. Baddeley, M. S. Tikhov, and R. M. Lambert, Structural and electronic properties of Sn overlayers and Pd/Sn surface alloys on Pd(111), Surf. Sci. **373**, 195 (1997).

[22] A. Pancotti, A. de Siervo, M. F. Carazzolle, J. J. Silva, P. A. P. Nascente, and R. Landers, Surface structure characterization by X-ray photoelectron diffraction of Sn ultra-thin films deposited on Pd(111), Surf. Sci. **685**, 7 (2019).

[23] C. Tayran and M. Çakmak, Electronic structure of the Pd₂Sn surface alloy on Pd(111)-($\sqrt{3}\times\sqrt{3}$)R30°, Eur. Phys. J. B **92**, 240 (2019).

[24] M. Inoue, S. Tanaka, J. Yuhara, and K. Morita, Ion impact desorption of metal atoms from Si(111)-$\sqrt{3}\times\sqrt{3}$-metal surfaces, Nucl. Instrum. Methods. Phys. Res. Sect. B. **58**, 411 (1991).

[25] S. Smidstrup, T. Markussen, P. Vancraeyveld, J. Wellendorff, J. Schneider, T. Gunst, B. Verstichel, D. Stradi, P. A. Khomyakov, U. G. Vej-Hansen, M.-E. Lee, S. T. Chill, F. Rasmussen, G. Penazzi, F. Corsetti, A. Ojanperä, K. Jensen, M. L. N. Palsgaard, U. Martinez, A. Blom, M. Brandbyge, and K. Stokbro, QuantumATK: An integrated platform of electronic and atomic-scale modelling tools, (https://www.synopsys.com/silicon/quantumatk.html), J. Phys. Condens. Matter **32**, 015901 (2020).

[26] M. J. van Setten, M. Giantomassi, E. Bousquet, M. J. Verstraete, D. R. Hamann, X. Gonze, and G.-M. Rignanese, The PseudoDojo: Training and grading a 85 element optimized norm-conserving pseudopotential table, Comput. Phys. Commun. **226**, 39 (2018).

[27] J. P. Perdew, A. Ruzsinszky, G. I. Csonka, O. A. Vydrov, G. E. Scuseria, L. A. Constantin, X. Zhou, and K. Burke, Restoring the Density-Gradient Expansion for Exchange in Solids and Surfaces, Phys. Rev. Lett. **100**, 136406 (2008).

[28] S. Smidstrup, D. Stradi, J. Wellendorff, P. A. Khomyakov, U. G. Vej-Hansen, M.-E. Lee, T. Ghosh, E. Jónsson, H. Jónsson, and K. Stokbro, First-principles Green's-function method for surface calculations: A pseudopotential localized basis set approach, Phys. Rev. B **96**, 195309 (2017).

[29] See Supplemental Material at http://link.aps.org/supplemental/10.1103/PhysRevMaterials.5.053403 for close-up STM image taken at a negative sample bias of the stanene layer in filled state.